CIRP Journal of Manufacturing Science and Technology 69 (2026) 158–168

Contents lists available at ScienceDirect

CIRP Journal of Manufacturing Science and Technology

journal homepage: www.elsevier.com/locate/cirpj

Full-length article

Modeling process-microstructure relations in PBF-LB/M laser treatment using Gaussian process surrogates, Bayesian optimization and eddy current sensing

Jork Groenewold [a,*], David Mai [a], Florian Stamer [b], Gisela Lanza [a]

[a] wbk Institute of Production Science, Karlsruhe Institute of Technology (KIT), Kaiserstr. 12, 76131 Karlsruhe, Germany
[b] Institute for Production Technology and Systems, Leuphana University Lüneburg, Universitätsallee 1, 21335 Lüneburg, Germany

ARTICLE INFO

Keywords:
Gaussian process surrogate models
Bayesian optimization
Laser treatment
Microstructure
Retained austenite
PBF-LB/M
Residual stress

ABSTRACT

A key challenge in additive manufacturing is the precise manipulation of microstructural properties to mitigate issues such as residual stresses and poor mechanical performance. In this context, laser treatments such as laser heat treatment and laser remelting offer a promising approach to influence microstructure in the process of powder bed fusion with laser beam melting (PBF-LB/M). However, the complex process-microstructure relationship remains insufficiently characterized for systematic process control.

This work presents a novel approach for efficient modeling of this relationship using Bayesian optimization (BO) with Gaussian process (GP) surrogate models. It addresses the mentioned issues by integrating BO with on-machine eddy current (EC) sensing, where the EC phase angle serves as an indirect metric for microstructural changes, such as the retained austenite content in the H13 tool steel used in this work. The BO algorithm adaptively proposes laser treatment parameters based on the GP surrogate model and an Upper Confidence Bound (UCB) acquisition function, iteratively refining the process-microstructure mapping.

The effectiveness of this approach was validated through two experiments that successfully manipulated the EC angle and thereby the retained austenite content, as confirmed by X-ray diffraction reference measurements. The trained GP model achieved high predictive accuracy with R^2 values up to 0.95, demonstrating its suitability as a process model for targeted microstructure modification via laser treatment in PBF-LB/M machines.

1. Motivation

Additive manufacturing (AM) processes, particularly powder bed fusion with laser beam melting (PBF-LB/M), are known to produce complex microstructures that significantly influence the mechanical properties of the final part [1,2]. In H13 tool steel, this complex microstructure is closely linked to the residual stress state. The origin of this link lies in the low-temperature martensitic transformation characteristic of H13: during PBF-LB/M, martensite forms upon rapid cooling at temperatures typically below 350 °C [3], at which point the surrounding material is already comparatively stiff. The volumetric expansion associated with the austenite-to-martensite transformation is therefore constrained, generating residual stresses in the surrounding matrix [3]. These residual stresses pose a critical challenge, which can lead to part warping, cracking, and a reduced fatigue life. Therefore, it is crucial to understand and control the microstructure, as variations such as the content of retained austenite play a key role in determining the residual stress state and overall mechanical performance of PBF-LB/M components [4,5].

Previous studies have highlighted the severity of these challenges. For instance, Narvan et al. [4] observed high tensile residual stresses, up to 400 MPa, in PBF-LB/M-produced H13 steel, which correlated with a microstructure composed of martensite, retained austenite, and various carbides. To mitigate these issues, researchers have explored various methods such as preheating the build plate or build chamber [2], optimizing process parameters and scan strategies [6–8], or controlling cooling temperature gradients using dual-laser PBF-LB/M machines [9]. While these approaches can partially reduce residual stress, they have not been effective in eliminating them completely, require significant additional time, or are not applicable on industrial machines.

Another approach is the laser treatment of fabricated layers before building subsequent layers: Methods such as laser heat treatment [10,11], laser remelting [5,12,13], and laser shock peening [14–16] have shown to influence microstructure and residual stresses in other applications. Although these laser-based methods exist, the precise control is

---

* Corresponding author.
E-mail address: jork.groenewold@kit.edu (J. Groenewold).

https://doi.org/10.1016/j.cirpj.2026.05.005
Received 18 December 2025; Received in revised form 17 April 2026; Accepted 19 May 2026

complicated by high parameter sensitivity and the typically unknown initial state of the manufactured material.

This inherent complexity makes it impossible to predetermine optimal process parameters prior to manufacturing; instead, adaptive adjustments must be performed on a layer-by-layer basis during the manufacturing process. Consequently, such an approach needs integrated, on-machine measurement capabilities. Previous work by the authors has demonstrated that eddy current (EC) sensing is well-suited for this purpose, as it provides a non-destructive means of monitoring microstructural states during fabrication [17]. However, the relationship between laser treatment parameters and the resulting microstructure remains insufficiently characterized for systematic process control. Therefore, the next step and objective of this work is to establish a model that captures the complex mapping between laser treatment parameters and the resulting microstructural state, as measured by EC sensing.

The paper is structured as follows: It begins with a review of the state of the art concerning laser heat treatment, laser remelting, in-process eddy current sensing in PBF-LB/M, and existing approaches used for modeling the related process-microstructure-relationships. Following this, the objectives and methodology are detailed, which include the experimental setup, system architecture implementation, optimization strategy and reference measurements for validation. We then present and discuss the results of the optimization, followed by a discussion of the limitations of our approach. Finally, the paper concludes with a summary of the findings and an outlook on future work.

2. Literature review

2.1. Laser-based approaches for microstructure modification

In this work, laser treatment is employed to modify the microstructure and thereby influence the resulting residual stress. Several types of laser treatment exist, which can be classified according to DIN 8580 as processes for “changing material properties”. According to Hügel et al. [18], laser-based methods that rely purely on thermal or mechanical effects without the addition of material include laser heat treatment, laser remelting, and laser shock peening. The latter requires high-energy pulsed lasers, which are not available in industrial PBF-LB/M systems, and is therefore not considered further.

In laser treatment processes, generally the following parameters can be varied: laser power P [W]; scanning speed v [mm/s]; laser beam radius [mm], spot size d [mm^2] or focus distance f [mm]; and for some processes hatch distance h [mm]. From these primary parameters, quantities such as the laser energy density $E = P/(v \cdot d)$ [J/mm^2] can be derived. Additionally, multiple treatment passes may be applied.

Depending on the selected parameter combination, the resulting thermal cycle either induces surface heat treatment or complete surface remelting. The following sections review corresponding approaches focusing on their ability to modify the microstructure, the underlying mechanisms, and the degree of controllability, i.e., the extent to which the resulting microstructure can be adjusted by process parameters.

2.1.1. Laser heat treatment

Laser heat treatment aims to locally modify the microstructure through controlled heating and self-quenching due to the rapid dissipation of heat into the surrounding material. Kostov et al. [10] investigate laser heat treatment of AISI 4140 (42CrMo4) using a continuous-wave laser ($P = 6$ kW, $d = 7.5 \times 7.5$ mm^2). The study reveals that even a single laser pulse produced a fully martensitic layer at the treated surface. Additional pulses have negligible influence on the microstructure, suggesting that the dominant mechanism was the austenite-to-martensite transformation triggered by rapid self-quenching. However, the systematic dependence on process parameters is not explored, and thus controllability remains unquantified.

In contrast, Telasang et al. [11] study laser heat treatment of H13 tool steel under varying laser energy densities and identified distinct regimes of microstructural evolution. At low energy densities between 22 J/mm^2 and 50 J/mm^2, no significant hardening occurs and the microstructure consists primarily of tempered martensite and fine carbides. Intermediate energy densities between 50 J/mm^2 and 75 J/mm^2 result in a martensitic surface layer formed through austenitization and subsequent self-quenching. At higher energy densities above 75 J/mm^2, surface melting occurs, leading to an inhomogeneous microstructure composed of ferrite, retained austenite, and carbides. These findings demonstrate that the microstructure strongly depends on the applied energy density and, consequently, on the thermal cycle induced by the laser. Laser heat treatment therefore provides a degree of controllability, as process parameters such as laser power and scan speed can be tuned to achieve specific microstructural states.

2.1.2. Laser remelting

Laser remelting involves complete surface melting and resolidification, producing distinct thermal histories compared to laser heat treatment.

Preußner et al. [12] examine laser remelting on H11 (1.2343) tool steel with laser powers ranging from 65 W to 320 W, spot diameters between 150 and 800 μm, and up to 16 remelting passes. The retained austenite content initially increases to approximately 30%–40% with rising power and beam diameter but decreased again to 5%–10% at very high values. The authors attribute this non-linear behavior to variations in the cooling rate: larger beam diameters result in lower cooling rates and consequently reduced retained austenite fractions. Multiple remelting passes also affect the phase balance, though the effect depends on both laser power and focus diameter. These results indicate that the retained austenite fraction can be tailored through process parameter selection, suggesting a relatively high degree of controllability.

Rezayat et al. [13] investigate the effect of laser remelting on stress-relieved AISI 301LN using a nanosecond pulsed laser. The study varies the laser power between 53.6 W and 63.3 W and the scan speed between 1.2 mm/s and 6 mm/s. The martensite content increases from 11.5% in the base material to 18.4% at the highest laser power and lowest scan speed, which is attributed to a higher cooling rate. This finding confirms that both laser power and scan speed critically influence the local cooling behavior and, consequently, the martensitic transformation. Thus, careful parameter control enables precise adjustment of the resulting microstructure.

A further investigation by Zhang et al. [5] examines laser remelting of H13 tool steel with laser energy densities between 90 and 120 J/mm^2. Increasing energy density leads to complete austenitization in the remelted zone, accompanied by coarser microstructures and enhanced carbide formation, while the martensite fraction decreases. Although retained austenite is not quantified, the study confirms that the cooling rate determines the balance between martensite and retained austenite formation. Consequently, the laser energy density constitutes a key parameter for microstructural control in laser remelting.

2.2. Process–microstructure modeling approaches

Establishing a quantitative link between process parameters and the resulting microstructure is essential for process control in laser treatment. Developing such models is particularly challenging due to several practical constraints: experiments are costly and time-consuming, material properties are often unknown, multiple process parameters may interact in non-linear and interdependent ways, and the resulting model must be sufficiently fast to enable on-machine microstructure control. The following sections review modeling approaches that aim to address these challenges.

2.2.1. Physics-based models

Physics-based models describe process-microstructure relationships using governing equations for heat transfer, melt pool dynamics, phase transformations, and stress evolution. They can be further classified into analytical models and numerical models, such as finite-element (FE) simulations. A representative example is the study by Schüßler et al. [19], in which hardness, residual stress, and phase composition were predicted using a thermo-mechanical FE model that incorporates geometry, phase-dependent material behavior, and laser interaction.

Physics-based models offer interpretable results and allow mechanistic exploration of parameter interactions. However, they exhibit several limitations: accurate material parameters are required, the simulations are computationally expensive, and, due to their high computational cost, these models are generally not suitable for on-machine control.

2.2.2. Data-driven models

In contrast, data-driven models infer the relationship between process parameters and microstructural outcomes directly from experimental data. Successful application requires an efficient strategy for data acquisition and appropriate modeling techniques to extract meaningful relationships.

To efficiently cover the process space with minimal experiments, classical design-of-experiment (DoE) approaches such as Central Composite Design (CCD) [20] or Latin Hypercube Sampling (LHS) [21] are commonly employed. These strategies enable systematic exploration and provide a basis for initial model training. However, as the number of process parameters increases, the required number of experiments grows rapidly, and initial designs may fail to capture complex, non-linear interactions not anticipated a priori.

After data acquisition, models map input parameters to target features using statistical techniques. Linear or polynomial regression models provide a simple first approach, whereas more flexible methods such as neural networks can capture complex, non-linear interactions. For example, Chen et al. [22] demonstrate multiple regression of laser-hardened microhardness based on CCD-designed experiments, achieving a maximum prediction error of approximately 4%. While effective, such approaches require sufficient data coverage; in high-dimensional parameter spaces, the number of experiments needed can become prohibitive.

Data acquisition and model training can also be combined in an iterative approach, where, based on data from few experiments, models are trained and used to select the next experiment that likely maximizes information gain. Bayesian Optimization (BO) is the most prominent example, often implementing a Gaussian Process (GP) as surrogate model, and an acquisition function to iteratively select promising experiments [23,24]. For example, Menold et al. [25] apply BO to laser welding, cutting, and polishing, efficiently identifying optimal process settings despite a high number of parameters. The resulting GP surrogate models can be directly applied for process control, as illustrated by Kocijan and Grancharova [26]. Other iterative strategies, such as active learning, focus on efficiently learning the mapping rather than optimizing a specific target [27]. These iterative approaches effectively address the main constraints: they reduce the number of expensive experiments, do not require a priori material data, can efficiently handle multiple parameters and non-linear interactions, and once trained, provide fast predictions suitable for near real-time control.

2.3. In-process eddy current sensing in PBF-LB/M

The eddy current measurement technique is fundamentally capable of assessing the microstructure in metal parts during manufacturing processes. According to Silva et al. [28], the martensite content in AISI 321 stainless steel during cold rolling correlates directly with the impedance phase angle, validated against X-ray diffraction and vibrating sample magnetometry. Asadi et al. [29] agrees with this finding, noting that higher martensite content corresponds to a lower phase angle and impedance. In contrast, Shaira et al. [30] found no correlation with the phase angle but instead with the signal amplitude. More recently, Fricke [31] established a correlation between the retained austenite content and the 3rd harmonic of the signal during the martensitic transformation of 1.4301 steel, with a measurement uncertainty below 2% for austenite contents exceeding 5%. While the precise signal feature that best captures phase composition appears to be material- and setup-dependent, the body of evidence consistently supports the use of eddy current signals as an indirect microstructure metric.

Eddy current sensors have also been successfully integrated into PBF-LB/M machines, though initially for purposes other than microstructure assessment. Todorov et al. [32] demonstrated measurement during the recoating step and correlated the data with defects and discontinuities. Spurek et al. [33] showed that relative density and lift-off can be separated from the measurement signal. Subsequent studies extended these approaches to broader density monitoring and defect detection [34–36].

The application of in-process eddy current sensing specifically for microstructure characterization in PBF-LB/M remains largely unexplored. Groenewold et al. [17] demonstrated the technical integration of an EC sensor into an industrial PBF-LB/M machine and provided initial evidence that the EC signal responds to laser-treatment-induced microstructural changes in H13 tool steel. Building on the general correlation established in the literature and this initial experimental evidence, the present work employs the EC phase angle as an indirect metric for microstructural state.

2.3.1. Summary

Across all reviewed studies, laser-based methods such as laser heat treatment and laser remelting have been demonstrated to enable local modification of microstructure through thermally driven mechanisms. The dominant mechanisms are the austenitization and self-quenching process that leads to martensitic transformation in laser heat treatment, and the melting and resolidification processes in laser remelting, which alter the phase balance between martensite, retained austenite, ferrite, and carbides. The resulting microstructure depends strongly on the local energy density and the associated cooling rate. Previous work by the authors has demonstrated that laser treatment can be implemented directly within an industrial PBF-LB/M system and is able to influence retained austenite content, confirming the feasibility of microstructural modification in PBF-LB/M machines [17]. The ability to adjust the microstructure via process parameters, is qualitatively demonstrated in most studies but remains quantitatively uncharacterized. Predictive models have yet to be established.

To model the relationship between laser treatment process parameters and the resulting microstructure, both physics-based and data-driven approaches were considered. While physics-based models offer interpretability and insights into the underlying mechanisms, data-driven models provide the significant advantage of being applicable even in the absence of detailed material properties. They also require less computational effort and are generally fast enough to be integrated into on-machine feedback control. To address the high experimental effort, iterative methods such as Bayesian Optimization (BO) can be employed, enabling the acquisition of substantial knowledge about the relationship between process parameters and target properties with only a few targeted experiments.

Furthermore, the literature review demonstrates that eddy current sensing provides a viable approach for indirect, on-machine characterization of microstructural state within the PBF-LB/M process.

In conclusion, the preceding analysis highlights the absence of an approach that combines laser treatment for microstructural modification with efficient iterative data-driven modeling, which would enable the targeted manipulation of microstructure within the PBF-LB/M process.

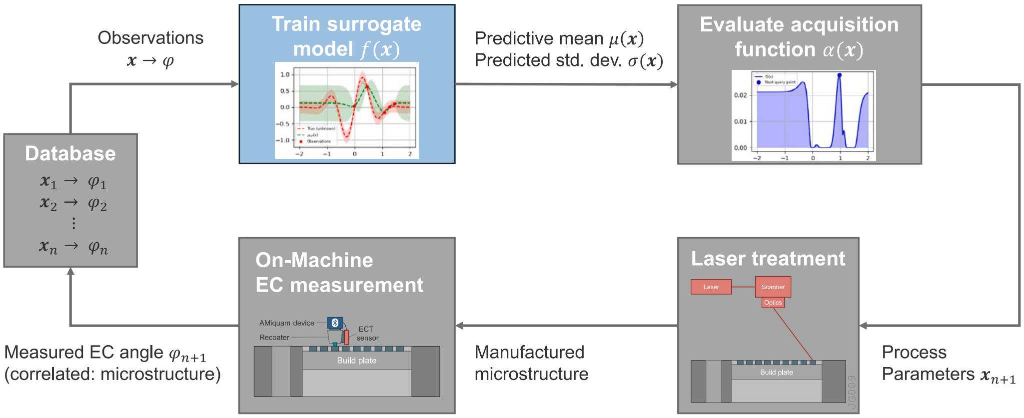

Fig. 1. Iterative BO process used for training process-material surrogate model.

3. Objectives and methodology

The literature review highlights the potential of laser treatment as a promising approach for targeted microstructure modification. However, achieving precise control over the microstructure requires accurate adjustment of process parameters, which remains a significant challenge. Given the complexity of the process-microstructure relationship and the absence of physical models, in this work an iterative data-driven method is the most viable modeling approach. To enable the application of such methods, integrated on-machine measurement systems are essential for characterization of microstructural changes within the PBF-LB/M machine.

In previous work, the authors demonstrated the feasibility of influencing microstructural properties through integrated laser treatment in PBF-LB/M systems, and provided initial evidence that on-machine EC sensing responds to the resulting microstructural changes [17]. Based on this evidence and the correlation between EC signals and phase composition established in the literature (Section 2.3), the EC phase angle is employed here as an indirect metric for microstructural state.

Building on this foundation, the present work aims to establish a quantitative mapping between laser treatment parameters $\mathbf{x}$ and the resulting microstructure, as indicated by the EC phase angle φ. Given the challenges outlined in the literature review, BO emerges as the most promising empirical approach for efficiently modeling this process-microstructure relationship.

Therefore, the primary objective of this work is to train a process-microstructure surrogate model using BO that captures the relationship between laser treatment parameters $\mathbf{x}$ and the resulting microstructure, as measured by the EC phase angle φ. The iterative approach is illustrated in Fig. 1. Initially, a surrogate model is trained on prior observations $\mathbf{x} \rightarrow \varphi$. An acquisition function then identifies unexplored regions of the parameter space based on the predictive mean $\mu(\mathbf{x})$ and standard deviation $\sigma(\mathbf{x})$ of the surrogate model, thereby determining a promising set of process parameters $\mathbf{x}_{n+1}$ for the next laser treatment experiment. The resulting microstructure is characterized using on-machine EC measurements, yielding the EC phase angle φ_{n+1}, which, as previously mentioned, correlates with the microstructure. The surrogate model is subsequently updated with the new observation $(\mathbf{x}_{n+1}, \varphi_{n+1})$, and the iteration continues.

Based on this iterative training approach and our goal to systematically investigate the limits of the effect of laser parameters on the EC angle across a wide parameter space, we conduct two separate experiments: one aimed at maximizing the EC angle and another focused on minimizing it. Based on the evidence reviewed in Section 2.3 and the initial findings of Groenewold et al. [17], the EC angle is expected to inversely correlate with the retained austenite content, which serves as a quantitative metric for microstructural assessment.

In the following sections, we explain our experimental setup and hardware (Section 3.1), the system architecture and automation solution (Section 3.2), the optimization methodology (Section 3.3), and the reference measurements (Section 3.4) in detail.

3.1. Experimental setup and hardware

The experimental setup is built around an SLM® 280 HL additive manufacturing system from Nikon SLM Solutions. The material chosen for the experiments is H13 tool steel (X40CrMoV5-1, 1.2344) due to its microstructural properties, i.e. its capability to form martensitic and austenitic material phases depending on the thermal history [5]. The PBF-LB/M system features a 400 W laser and a variable focus shift. It operates in a closed argon atmosphere with a build plate preheating temperature of up to 200 °C, which has been shown to improve the density of test specimens according to Narvan et al. [4]. The manufacturing parameters for the specimens were optimized using the design of experiments method, resulting in a layer thickness of 30 µm, a laser power of 250 W, a scan speed of 750 mm/s, a hatch distance of 0.09 mm, and a laser focus of −4 mm. The specimens were cuboidal, with dimensions of 8 mm × 10 mm × 6 mm (length × width × height).

For the on-machine measurements, an eddy current system from AMiquam SA with two sensors was integrated into the machine's recoater system, as depicted in Fig. 2. The sensors are positioned at a height of 0.2 mm above the part, and the data is transmitted wirelessly via Bluetooth to an external measurement computer. The EC angle serves as the optimization target and an indirect measure of the retained austenite content. Lower EC angle values in the additively manufactured parts suggest an increased retained austenite content.

The measurement depth of eddy current testing is governed by the skin effect, quantified by the penetration depth δ [37]:

$$\delta = \frac{1}{\sqrt{\pi f \sigma \mu_0 \mu_r}} \tag{1}$$

The sensor operates at $f = 200\,\text{kHz}$. Material parameters for H13 are taken from the manufacturer datasheet and estimated from literature as detailed in Appendix, yielding $\sigma = 1.92 \times 10^6$ S/m and $\mu_r \approx 45$ (range: 35–55). The permeability of free space is $\mu_0 = 4\pi\ 10^{-7}$ H/m [37]. Substituting into Eq. (1) yields a penetration depth of $\delta = 110\,\mu\text{m}$. For $\mu_r = 35$–55, δ ranges from 100–130 µm. The eddy current measurement is thus sensitive to the microstructure within approximately 100–130 µm of the surface.

The laser treatment parameters were controlled by the BO algorithm within defined operational limits. These bounds were selected based on the machine's technical capabilities and preliminary tests to avoid process instabilities such as excessive heat accumulation or insufficient energy input. The parameter ranges used in this study are summarized in Table 1.

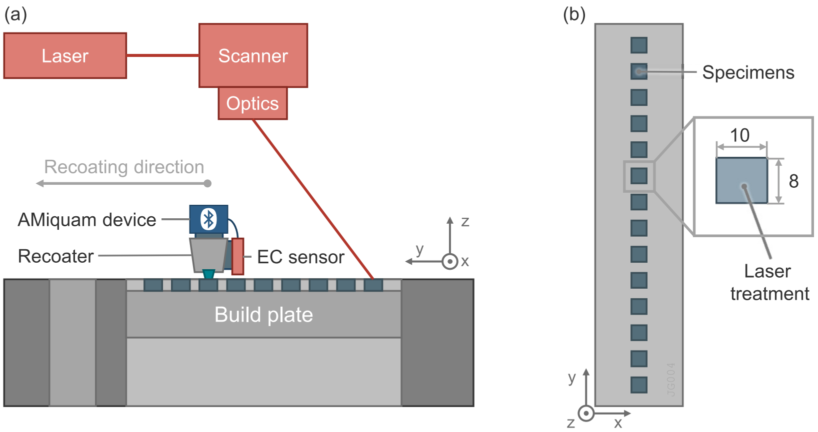

Fig. 2. Integration of the on-machine eddy current sensor system from AMiquam into the SLM® 280 HL machine (a) and arrangement of test specimens on the build plate (b).

Table 1
Operational limits for laser treatment parameters.

Limit	P [W]	v [mm/s]	f [mm]	h [mm]
Minimum	20	150	−10	0.008
Maximum	200	300	0	0.2

3.2. System architecture and automation

The system architecture implements a fully automated, iterative measurement and parameter optimization framework. The communication infrastructure, illustrated schematically in Fig. 3, consists of the PBF-LB/M machine computer and a separate measurement computer, which are interconnected through wireless and wired connections for data transfer and status exchange.

On the PBF-LB/M machine computer, Python-based interface software utilizing PyAutoGUI controls the proprietary Manufacturing Software Controller (MSC). Following each laser treatment step, specimens undergo EC measurement, with the data transmitted via Bluetooth to the measurement computer and the completion status confirmed through WebSocket. The measurement computer hosts the BO model and performs EC data processing. It analyzes the acquired EC data to compute the resulting EC angle and determines the subsequent laser treatment parameters using the BO algorithm. These optimized parameters are transmitted back to the PBF-LB/M machine computer via a Flask-based REST API, triggering the next iteration automatically.

3.3. Optimization methodology

In this work, BO is employed, which requires three components: (1) an approach for generating an initial set of parameters and data to initialize the surrogate model, (2) a surrogate model that captures the relationship between process parameters and observed outcomes and (3) an acquisition function that determines the next sampling point based on that surrogate model.

First, for initial data generation, latin hypercube sampling (LHS) with 11 sampling points is used to efficiently cover the multidimensional design space with a small, well-distributed set of initial samples $\mathcal{D}_n = \{(\mathbf{x}_i, \varphi_i)\}_{i=1}^{n}$, where $\mathbf{x}_i$ denotes the process parameters and φ_i the corresponding objective value, i.e. the EC phase angle.

Secondly, the surrogate model $f(\mathbf{x})$ is then trained on the previously observed data $\mathcal{D}$. As surrogate model a GP is used [23]:

$$f(\mathbf{x}) \sim \mathcal{GP}\left(m(\mathbf{x}), k(\mathbf{x}, \mathbf{x}')\right) \tag{2}$$

where $m(\mathbf{x})$ is the mean function and $k(\mathbf{x}, \mathbf{x}')$ the covariance kernel. After conditioning on the observed data, the GP provides a predictive mean $\mu(\mathbf{x})$ and standard deviation $\sigma(\mathbf{x})$ for any new parameter configuration [23].

Thirdly, the selection of the next sampling point is governed by the acquisition function. In this work, the *Upper Confidence Bound* (UCB) criterion is used due to its simplicity and strong theoretical convergence guarantees. By adjusting its parameter β, it balances the trade-off between exploring new parameter spaces (high β) and exploiting known optimal regions (low β) [23]:

$$\alpha_{\mathrm{UCB}}(\mathbf{x}) = \mu(\mathbf{x}) + \sqrt{\beta}\,\sigma(\mathbf{x}) \tag{3}$$

The next experimental setting $\mathbf{x}_{n+1}$ is determined by maximizing the acquisition function [23]:

$$\mathbf{x}_{n+1} = \arg\max_{\mathbf{x}} \alpha_{\mathrm{UCB}}(\mathbf{x}) \tag{4}$$

For each iteration, the GP model is retrained with the updated dataset, and the optimization continued until convergence of the objective value, i.e. the EC angle, is observed.

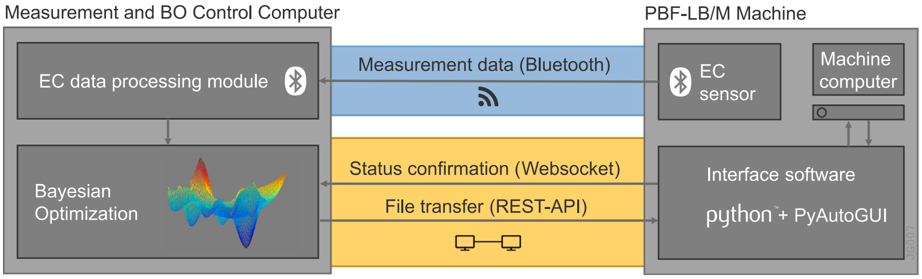

Fig. 3. Schematic of the communication architecture for employing BO of laser treatments on the PBF-LB/M machine.

3.3.1. Model evaluation

To assess the quality of the surrogate model, both deterministic and probabilistic performance metrics are computed for all evaluated samples. The deterministic metrics quantify the accuracy of the predicted mean values $\mu(\mathbf{x})$ relative to the observed EC angles φ, while the probabilistic metrics evaluate the calibration of the predictive uncertainties $\sigma(\mathbf{x})$.

As deterministic metrics, we compute Root Mean Squared Error (RMSE) as the average magnitude of prediction errors, Mean Absolute Error (MAE) as a robust measure of the typical prediction error, and the Coefficient of Determination (R^2) as an indication of the proportion of variance in the observed data captured by the model.

As a probabilistic metric, we compute the empirical coverage, which is calculated as the fraction of observed values lying within the predicted confidence intervals (e.g., 90% and 95%) [38]:

$$C_\alpha = \frac{1}{N}\sum_{i=1}^{N} \mathbf{1}\left\{ \varphi_i \in \left[\mu(\mathbf{x}_i) \pm z_{\alpha/2}\sigma(\mathbf{x}_i)\right] \right\} \tag{5}$$

where $z_{\alpha/2}$ is the standard normal quantile corresponding to the desired confidence level.

3.4. Reference measurements

To validate the effect of the optimization on microstructural changes, X-ray diffraction (XRD) measurements are carried out on selected test specimens after the optimization and post-processing steps. The measurements are conducted using a Stresstech XStress DR45 system equipped with a Cr-Kα radiation source operated at 30 kV and 9 mA and using a 1 mm collimator.

For each test specimen, three measurement points are taken: one at the center and two at positions ±2.5 mm from the center. At each position, the retained austenite content is determined from the integrated intensities of four diffraction peaks (Fe_{211}, Fe_{200}, γ_{200}, γ_{220}); the instrument computes the mean and standard deviation across the four peak-based estimates as an indicator of measurement consistency. The retained austenite content per specimen is then quantified by computing a weighted mean and weighted standard deviation across these three measurements, reflecting the spatial variability of retained austenite content across the measurement positions.

4. Results

The following section presents the results of the two primary optimization experiments, focusing on the performance of the BO loop, the accuracy of the GP models, the reproducibility of the outcomes and the validation of microstructural change.

4.1. Optimization performance

Two experiments are conducted to evaluate the optimization's ability to manipulate the EC angle.

The first experiment focuses on maximizing the EC phase angle to identify laser treatment parameters that reduce retained austenite content. The BO loop was initialized with LHS to provide diverse training data for the GP surrogate. An Upper Confidence Bound acquisition function was employed with an exploration-promoting schedule: β was set to high values (between 4.0 and 6.0) in the early iterations to encourage exploration of the parameter space and was reduced progressively, reaching $\beta = 2.0$ at iteration 30 and $\beta = 0.5$ at iteration 40 to promote exploitation of promising regions.

The Convergence behavior is shown in Fig. 4 by the best-so-far value of optimization, the evolution of the objective value, the predicted mean of the GP model and its predicted standard deviation. During the initial phase the objective values exhibited large variability as the optimizer explores different regimes. After the scheduled reduction of β the search concentrates on locally promising configurations and convergence accelerated (also see Fig. 4). Over the full run, the highest EC angle observed was 0.043 rad, corresponding to an improvement of approximately 48% relative to the EC angle range sampled during the LHS initialization.

The model's predicted mean values and uncertainty, represented by the standard deviation, are also shown in Fig. 4. The progressive reduction in predicted uncertainty over iterations indicates increasing model confidence in the explored parameter regions. This behavior aligns with the expected convergence of the BO process, where the surrogate model becomes more certain as it gathers more data in promising areas of the parameter space. However, while the predicted mean values follow the objective value closely in the first iterations, some divergence is observed in later iterations.

The second experiment aims to minimize the EC angle to identify parameters that promote significant microstructural change and increase retained austenite content. The convergence behavior is illustrated in Fig. 5, showing the best-so-far value of the optimization and the evolution of the objective value over iterations. The Upper Confidence Bound (UCB) acquisition function again is initially configured with a high exploration factor ($\beta = 4.0$) and progressively reduced as the number of iterations increases to favor exploitation.

During the optimization process, a high variation in the objective values is observed across all iterations, reflecting the exploration of diverse parameter configurations. Over the course of the experiment, the lowest EC angle achieved was −0.03 rad, representing an improvement of 167% compared to the EC angle range sampled during the LHS initialization phase.

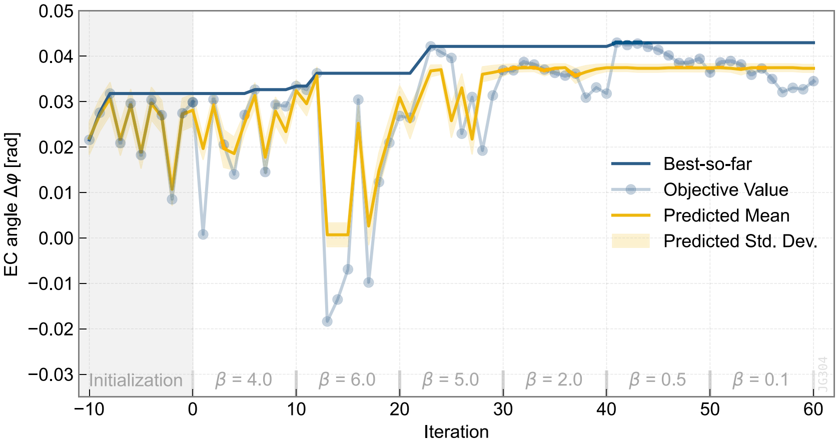

Fig. 4. Convergence behavior during the maximization of the EC angle.

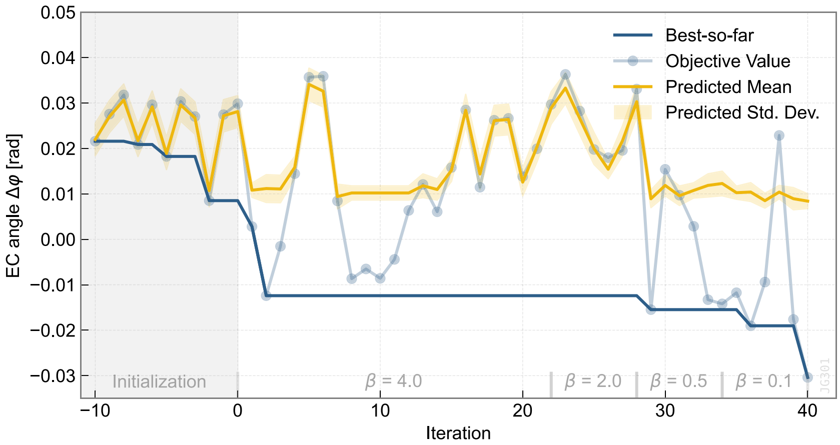

Fig. 5. Convergence behavior during the minimization of the EC angle.

However, the model's uncertainty, as seen in Fig. 5, remains higher and does not stabilize in the later iterations. This suggests that the surrogate model struggles to confidently predict outcomes in the explored parameter regions. The predicted mean values follow the objective value closely in the iterations where EC angles above 0 rad are observed, but diverge significantly in the lower EC angle regime.

The optimized laser treatment parameters for maximizing and minimizing the EC angle are summarized in Table 2. The results reveal that the two objectives require clearly different parameter combinations across laser power, scan speed, focus position, and hatch distance. For maximization, the optimization converges towards conditions associated with a comparatively lower thermal input per unit area, whereas the minimization solution shifts towards settings that increase the local energy density and intensify the thermal impact.

Table 2

Optimized laser treatment parameters for maximization and minimization of EC angle.

Objective	P [W]	v [mm/s]	f [mm]	h [mm]
Maximization	76.78	300.00	0.00	0.200
Minimization	92.73	205.82	−4.45	0.010

4.2. Model accuracy

To evaluate the performance of the surrogate models, predictions from the final GPs are compared to the measured EC angles across all evaluated parameter combinations. In addition, new GP models are retrained on maximization and minimization datasets as well as all available data in order to evaluate if model performance can be further improved. Table 3 summarizes the quantitative performance metrics for both the maximization, minimization and retraining surrogate models.

The deterministic metrics reveal a substantial difference in model quality between the two experiments. The maximization model achieves an R^2 of 0.80 with an RMSE of 0.0063 rad and MAE of 0.0043 rad, indicating a strong correlation between predictions and observations. In contrast, the minimization model exhibits an R^2 of only 0.35 with an RMSE of 0.014 rad and MAE of 0.0096 rad.

Table 3

Performance metrics for the maximization model (GP Max), minimization model (GP Min) and the models that have been retrained on maximization and minimization datasets and all available data (GP Ret).

Model	RMSE	MAE	R^2	$C_{95\%}$
GP Max	0.0063	0.0043	0.80	51.7%
GP Min	0.0140	0.0096	0.35	52.5%
GP Ret				
Max	0.0025	0.0018	0.96	69.6%
Min	0.0058	0.0039	0.89	88.2%
All	0.0038	0.0024	0.95	82.5%

The probabilistic metrics reveal a systematic miscalibration of uncertainty estimates in both models. The empirical coverage probabilities fall significantly below nominal levels: for the maximization model, $C_{95\%} = 51.7\%$, while for the minimization model, $C_{95\%} = 52.5\%$. These values indicate that the predicted confidence intervals are substantially narrower than the actual data scatter.

To evaluate whether the GP model can accurately fit the data, a retraining procedure is conducted using GP models with new data preprocessing.

In standard BO, normalization of the input space to the unit cube $[0,1]^D$ is commonly recommended to ensure consistent scaling across dimensions [39]. However, in our case, the distribution of input parameters is highly uneven due to the sampling behavior during optimization. This leads to a situation where min–max normalization becomes overly sensitive to outliers: a single extreme value can compress the remaining inputs into a narrow interval, reducing the effective variability available to the GP and making model fitting more challenging. To mitigate this issue, the retraining employs standardization, transforming each input dimension to zero mean and unit variance. This approach is less affected by uneven sampling, thereby preserving meaningful variations in the data. As a result, we expect improved model fit and a more reliable calibration of predictive uncertainty.

Table 3 includes the performance metrics for the retrained models. Retraining on the minimization dataset alone with parameter standardization improves R^2 from 0.35 to 0.89 and C_{95} from 52.5% to 88.2%, using identical data. The retrained maximization model similarly improves to $R^2 = 0.96$ and $C_{95} = 69.6\%$. The model retrained on all available data achieves $R^2 = 0.95$ and $C_{95} = 82.5\%$, indicating a more accurate calibration of the uncertainty estimates in the retrained model. Fig. 6 illustrates the predicted versus actual values for all trained models. The retrained GP models demonstrate a notably better fit to the data, whereas the earlier models exhibit lower prediction accuracy, particularly the minimization model, which had high prediction errors with low actual values.

However, the C_{95} values remaining below the nominal 95% and the deviations of the predictions from the retrained GP models show that either the models are not capable of fitting the data perfectly or there are sources of variability in the measurement or the process-microstructure relationship the models cannot account for.

4.3. Reproducibility test

To investigate potential sources of variability in the process-structure relationship and measurement system, a reproducibility test was conducted. This involved experiments on three separate build

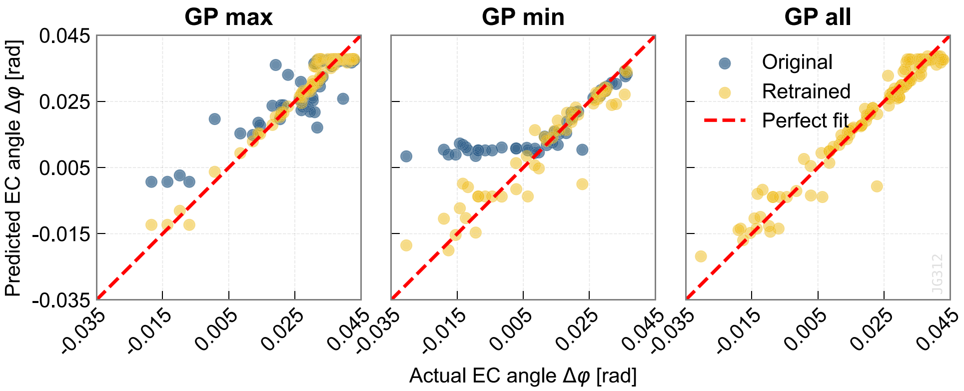

Fig. 6. Predicted vs. actual EC angle values for maximization, minimization GP models and all retrained GP models.

plates (Test 1–3) using identical process parameters, with the eddy current measurement device restarted after each build. Each build plate contained two specimens for analysis.

The results of the reproducibility test are summarized in Table 4. Across all tests, the maximum variation in EC angle observed was 0.0199 rad, while the maximum variation in retained austenite content was 4.4 percentage points. Within individual tests, the maximum variation in EC angle was reduced to 0.0052 rad, and the maximum variation in retained austenite content was 1.2 percentage points. Notably, the variations observed within individual tests were significantly lower than those observed across all tests: approximately 50% less for retained austenite content and about 75% less for EC angle.

Table 4
Maximum differences within each group for retained austenite content (RAC) and EC angle φ.

Group	RAC diff. [%-p.]	φ diff. [rad]
Test 1	1.2	0.0052
Test 2	0.1	0.0047
Test 3	0.2	0.0039
Overall	4.4	0.0199

4.4. Validation of microstructure optimization

To validate the effectiveness of the BO approach in manipulating microstructural properties, X-ray diffraction (XRD) measurements of retained austenite content were performed on the specimens produced during BO where the resulting EC angle was highest and lowest.

Fig. 7 presents the XRD results of these specimens. The specimens are categorized into two groups based on their respective optimization objectives. For each specimen, three XRD measurements were conducted at different positions corresponding exactly with the locations of the EC measurements. The retained austenite content for each specimen was determined by calculating the weighted mean and standard deviation.

Based on the established relationship between the EC phase angle and microstructural composition, an inverse correlation was expected: maximizing the EC angle should correspond to a reduction in retained austenite content, while minimizing the EC angle should lead to an increase. The experimental results confirm this hypothesis. Specimens optimized for maximum EC angle exhibited a significantly reduced mean retained austenite content, with a minimum of 9.4% (standard deviation 2.6%). Conversely, specimens optimized for minimum EC angle achieved a substantially higher retained austenite content, reaching a maximum of 26.8% (standard deviation 5.5%). These findings are in agreement with the initial assumptions regarding the relationship between the EC phase angle and retained austenite content, thereby validating the BO's capability to effectively control microstructural outcomes through systematic parameter optimization.

5. Discussion

The BO approach successfully identified process settings that yielded significant changes in the observed EC phase angle, spanning a total range from −0.03 rad to +0.043 rad. Reference measurements confirmed substantial variations in retained austenite content values between 9.4% and 26.8%.

However, certain issues regarding optimization performance and model accuracy warrant further investigation. Notably, the fit of the original maximization model was significantly better than that of the minimization model. The minimization model struggled to accurately capture data points with negative EC angles. Retraining new GP models revealed that the marked performance gap between the original maximization and minimization models ($R^2 = 0.80$ vs. 0.35) can be attributed to insufficient input parameter standardization in the initial training procedure. This is confirmed empirically by the retrained minimization model, which recovers $R^2 = 0.89$ on the identical dataset. The original model's failure to accurately represent negative EC phase

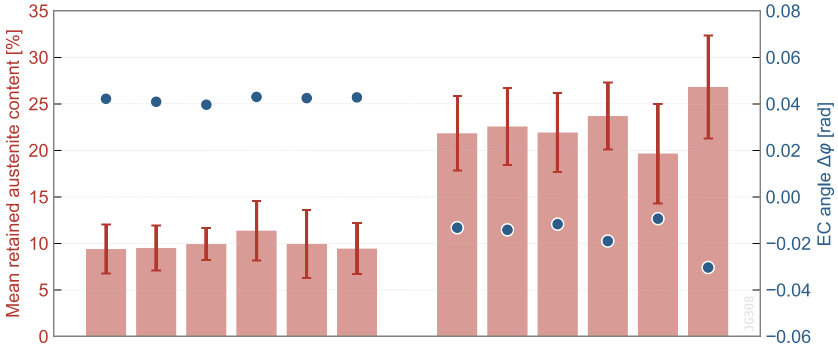

Fig. 7. Retained austenite content measured by XRD with corresponding EC angle for specimens produced with BO-optimized parameters.

angle values therefore reflects a numerical conditioning issue rather than a structural limitation of the GP surrogate or the underlying process-structure relationship.

Despite the improvements in the retrained GP models, a small prediction error remained in all retrained models with RMSE values ranging from 0.0025 rad (GP Ret Max) to 0.0058 rad (GP Ret Min), and empirical coverage C_{95} remained at 69.6%–88.2%, still below the nominal 95%. Considering the entire iterative framework, this issue may arise from variability in the process-microstructure relationship, measurement uncertainty, or other unknown sources.

To investigate variance in the process-microstructure-relationship, reproducibility tests with constant process parameters were done. The tests revealed that retained austenite content varies over multiple experiments, with a maximum variation of 4.4 percentage points, while the variance was relatively low within individual experiments, not exceeding 1.2 percentage points. This indicates that within one experiment, the behavior seems to be reproducible, but other unknown external factors seem to influence retained austenite content over multiple experiments. Besides, it is possible that the “process landscape” is smoother or more deterministic in some parts of the parameter space than in others, which was not tested in this work.

For investigating variance in the EC measurements, the EC angle results for the same reproducibility tests were compared. The test revealed that despite nearly identical retained austenite content, EC angle measurements deviated between runs, reaching a maximum variation of 0.0199 rad. However, within individual runs, deviation was observed but it was relatively small, with a maximum variation of 0.0052 rad. This indicates calibration issues between runs and some uncertainty of the measurement equipment within runs.

A further source of measurement uncertainty is related to the finite penetration depth of the eddy current signal. As established in Section 3.1, this depth is approximately 110 µm, whereas the depth of microstructural transformation induced by the laser treatment may be shallower. Due to the skin effect, the eddy current density decays exponentially with increasing depth [37], so that the measured signal represents a depth-weighted integral of the microstructure rather than a uniform sampling over the full penetration depth. If the laser-induced transformation does not extend throughout this entire depth, the signal is dominated by the modified near-surface region, with only a minor contribution from the underlying, unaffected material. Nevertheless, at very shallow transformation depths, this depth-weighting effect may additionally explain the observed discrepancy in model performance between the maximization and minimization experiments, as the effective sensing volume relative to the transformed volume would differ between the two parameter regimes.

Another potential source of uncertainty in the EC phase angle mapping is the magnetoelastic effect: residual stresses alter the magnetic permeability of ferromagnetic materials and thus influence the EC impedance signal [40]. Since different laser treatments can simultaneously modify both the retained austenite content and the residual stress state, a confounding influence on the phase angle cannot be excluded. Available literature suggests, however, that this influence is likely subordinate. Studies specifically examining the stress sensitivity of the EC phase angle report changes on the order of 0.006 rad per 100 MPa [41], which is small relative to the total EC angle span of approximately 0.07 rad observed in the present work, with the same authors finding that the impedance amplitude correlates more strongly with residual stress than the phase angle [42]. Furthermore, Fanlin et al. [40] report a frequency-dependent stress sensitivity of the phase angle below 3% at 200 kHz, corresponding to the excitation frequency employed in the present study. It should be noted, however, that both the measurement setups and the materials investigated in these studies differ from those used in the present work, which limits the direct applicability of the reported sensitivity values. A quantitative separation of microstructure composition and residual stress contributions to the measured EC phase angle was not feasible within the scope of this work and represents a subject for future investigation.

In summary, both process-structure relationship and measurement uncertainty contribute to overall variability. Given these issues and the imperfect data preprocessing procedure, it is explicable that the GP models underestimate predictive variance. The current BO and GP setup appears inadequate, as the predictive variance of the GP is too narrow to capture the inherent variability in the data.

For an improvement of the overall approach, three main directions can be identified: (1) enhancing the calibration procedure of the EC measurements and quantifying the influence of residual stress, (2) improving the preprocessing and uncertainty quantification of the GP model used for BO, and (3) investigating additional influencing factors that may affect retained austenite content:

- To enhance the calibration procedure of the EC measurements, it is important to account for the temperature of the EC sensor, as literature indicates that it plays a central role in measurement accuracy. Systematic calibration to known reference points between iterations could reduce overall measurement uncertainty. Additionally, factors such as porosity and surface roughness changes during remelting should be considered by conducting systematic experiments with reference measurements to identify and mitigate systematic errors.
  Furthermore, metallographic cross-sections should be examined to characterize the actual depth of the laser-induced microstructural transformation. If the transformation depth is found to be substantially smaller than the current penetration depth of ≈ 110 µm, adjusting the sensor excitation frequency to reduce the penetration depth would improve the spatial correspondence between the measurement volume and the transformed zone, thereby enhancing measurement sensitivity.
  To quantitatively assess the influence of residual stress on the measured EC phase angle, future work should include a systematic separation of microstructural and residual stress contributions to the impedance signal. This could be achieved by combining EC measurements with simultaneous microstructure and residual stress characterization on specimens with controlled and independently varying phase fractions and stress states.
- To improve the optimization performance, the standardization instead of normalization of the input data should be employed for data preprocessing, as the retrained GP model showed better predictive accuracy. Furthermore, the reproducibility tests revealed some variance in the retained austenite content, and it is unclear whether this variability is consistent across the entire process landscape. For this reason, it may be beneficial to investigate whether a heteroscedastic noise model could improve the uncertainty quantification of the GP during optimization. A heteroscedastic noise model explicitly accounts for input-dependent noise levels [23] and could, in principle, provide more accurate predictive variances, thereby potentially improving the guidance provided by the acquisition function.
- To investigate additional influencing factors affecting retained austenite content, the influence of temperature deviations during processing should be explored, potentially through the use of in-situ thermography to monitor and quantify thermal effects on microstructural evolution. Furthermore, it would be valuable to examine the potential impact of sample position due to incidence angle variations. Such data could subsequently be integrated into the BO approach.

Despite the imperfect results, the BO remains a promising method for guiding experimental design, as it effectively prioritizes promising parameter regions. The approach successfully identified new parameter sets that significantly influenced microstructural changes by both increasing and decreasing retained austenite content, with XRD-validated values ranging from a minimum of 9.4% to a maximum of 26.8%. The optimized parameters align well with theoretical expectations and findings from prior studies such as [12]. Specifically, for minimizing retained austenite content, the BO identified high scan speeds, moderate laser power, and large hatch distances, which promote rapid cooling rates conductive to martensite formation. Conversely, for maximizing retained austenite content, the BO selected higher laser powers, lower scan speeds, and smaller hatch distances, resulting in increased energy input and reduced cooling rates, thereby limiting martensite formation. Overall, the results underline that BO is a powerful tool to steer microstructural outcomes in laser treatment in metal additive manufacturing.

6. Conclusion

In the present study, a Gaussian Process (GP) surrogate model was trained to establish a quantitative mapping between laser treatment parameters and the resulting microstructure. Bayesian optimization (BO) was employed to efficiently train the GP model of this process-microstructure relationship by iteratively selecting laser parameters to maximize or minimize the EC phase angle, which serves as an indirect metric for microstructural changes. The main findings include:

- The approach successfully identified laser treatment parameters that significantly altered the EC phase angle.
- Validation using XRD measurements confirmed that a maximum retained austenite content of 26.8% and a minimum of 9.4% were achieved, demonstrating the ability of BO to steer microstructure through systematic adjustment of process parameters guided by EC measurement feedback.
- The trained GP model exhibited high predictive accuracy for maximization of the EC phase angle ($R^2 = 0.80$), while lower accuracy was observed for minimization ($R^2 = 0.35$). Both models systematically underestimated predictive uncertainty.
- Retraining a GP model on the available data using input-standardization instead of normalization exhibited high predictive accuracy ($R^2 = 0.95$) in both the maximization and minimization regime.
- Reproducibility tests revealed variance in process-microstructure relationship and measurement uncertainty that should be examined further.

Future work will focus on improving model performance through enhanced GP uncertainty quantification, refined EC measurement calibration, and investigation of additional influencing factors. Based on the established process-microstructure model, a closed-loop control framework for laser treatment in PBF-LB/M can be developed. The final objective is to influence residual stresses during PBF-LB/M manufacturing through localized microstructural modification via laser treatment, thereby enabling targeted control of the associated residual stress state.

CRediT authorship contribution statement

Jork Groenewold: Writing – original draft, Visualization, Validation, Methodology, Investigation, Formal analysis, Data curation, Conceptualization. **David Mai:** Writing – original draft. **Florian Stamer:** Writing – review & editing, Writing – original draft, Supervision. **Gisela Lanza:** Writing – review & editing, Supervision, Project administration.

Declaration of competing interest

The authors declare that they have no known competing financial interests or personal relationships that could have appeared to influence the work reported in this paper.

Acknowledgments

This research and development project is funded by the German Federal Ministry of Research, Technology and Space (BMFTR) within the “Future of Value Creation – Research on Production, Services and Work” program (funding number 02J23C100) and managed by the Project Management Agency Karlsruhe (PTKA). The authors are responsible for the content of this publication.

Appendix. Estimation of electric and magnetic properties of H13

Electrical Resistivity

The value $\rho = 0.52\,\Omega\,\mathrm{mm}^2/\mathrm{m}$ ($\sigma = 1.92 \times 10^6$ S/m) is taken from the manufacturer datasheet for H13 (X40CrMoV5-1).[1]

Relative Permeability

The relative permeability μ_r of H13 tool steel is not tabulated for bulk material and the as-built PBF-LB/M condition. The following estimation proceeds from reference data for plain Fe–C alloys reported by Bozorth [43], with successive corrections for alloy composition.

Reference values. Bozorth [43] reports initial permeability values of $\mu_i = 170$ (annealed) and $\mu_i = 70$ (oil-quenched) for Fe–C alloys at ≈ 0.4 wt% C, with base alloy impurities of ≤ 0.2 wt% Si and ≤ 0.6 wt% Mn. The initial permeability μ_i is the quantity relevant to eddy current excitation at low field amplitudes. The oil-quenched value $\mu_i = 70$ is the appropriate starting point, as the as-built PBF-LB/M microstructure is martensitic in character, with cooling rates far exceeding those of conventional oil quenching.

Correction for alloying elements. Bozorth [43] tabulates the reduction in magnetic induction per 1 wt% of each alloying element relative to a plain iron reference. Applying these reductions at to the nominal H13 composition (0.39 wt% C, 1.00 wt% Si, 0.38 wt% Mn, 5.15 wt% Cr, 1.35 wt% Mo) yields a combined reduction to approximately 64% of the plain iron reference induction. Scaling $\mu_i = 70$ accordingly gives:

$$\mu_r \approx 70 \cdot 0.64 \approx 45$$

A value of $\mu_r = 45$ is therefore adopted, with a conservative range of 35–55 reflecting uncertainties in the element-wise scaling at low field strengths.

References

[1] Narvan M, Al-Rubaie KS, Elbestawi M. Process-structure-property relationships of AISI H13 tool steel processed with selective laser melting. Materials 2019;12:2284. http://dx.doi.org/10.3390/ma12142284.

[2] Mertens R, Vrancken B, Holmstock N, Kinds Y, Kruth J-P, Humbeeck J Van. Influence of powder bed preheating on microstructure and mechanical properties of H13 tool steel SLM parts. Phys Procedia 2016;83:882–90. http://dx.doi.org/10.1016/j.phpro.2016.08.092.

[3] Yan JJ, Zheng DL, Li HX, Jia X, Sun JF, Li YL, Qian M, Yan M. Selective laser melting of H13: microstructure and residual stress. J Mater Sci 2017;52:12476–85. http://dx.doi.org/10.1007/s10853-017-1380-3.

[4] Narvan M, Ghasemi A, Fereiduni E, Kendrish S, Elbestawi M. Part deflection and residual stresses in laser powder bed fusion of H13 tool steel. Mater Des 2021;204:109659. http://dx.doi.org/10.1016/j.matdes.2021.109659.

[5] Zhang J, Yu M, Li Z, Liu Y, Zhang Q, Jiang R, Sun S. The effect of laser energy density on the microstructure, residual stress and phase composition of H13 steel treated by laser surface melting. J Alloys Compd 2021;856:158168. http://dx.doi.org/10.1016/j.jallcom.2020.158168.

[6] Kaess M, Werz M, Weihe S. Residual stress formation mechanisms in laser powder bed fusion—A numerical evaluation. Materials 2023;16:2321. http://dx.doi.org/10.3390/ma16062321.

[7] Hassila C-J, Malmelöv A, Andersson C, Hektor J, Fisk M, Lundbäck A, Wiklund U. Influence of scanning strategy on residual stresses in laser-based powder bed fusion manufactured alloy 718: modeling and experiments. Materials 2024;17:6265. http://dx.doi.org/10.3390/ma17246265.

---

[1] https://www.stauberstahl.com/fileadmin/Downloads/werkstoffe/Werkstoff-1.2344-Datenblatt.pdf, accessed 2026-04-02.

[8] Bernard A, Kruth J-P, Cao J, Lanza G, Bruschi S, Merklein M, Vaneker T, Schmidt M, Sutherland JW, Donmez A, Silva EJ Da. Vision on metal additive manufacturing: Developments, challenges and future trends. CIRP J Manuf Sci Technol 2023;47:18–58. http://dx.doi.org/10.1016/j.cirpj.2023.08.005.

[9] Searle S, Vanini M, Vanmunster L, Vrancken B. Parameter prediction and laser alignment for synergistic multi-laser powder bed fusion. Procedia CIRP 2024;124:82–8. http://dx.doi.org/10.1016/j.procir.2024.08.076.

[10] Kostov V, Gibmeier J, Wanner A. Local residual stress distributions induced by repeated austenite-martensite transformation via laser surface hardening of steel AISI 4140. Mater Sci Forum 2011;681:321–6. http://dx.doi.org/10.4028/www.scientific.net/MSF.681.321.

[11] Telasang G, Majumdar J Dutta, Padmanabham G, Manna I. Structure–property correlation in laser surface treated AISI H13 tool steel for improved mechanical properties. Mater Sci Eng: A 2014;599:255–67. http://dx.doi.org/10.1016/j.msea.2014.01.083.

[12] Preußner J, Oeser S, Pfeiffer W, Temmler A, Willenborg E. Microstructure and residual stresses of laser remelted surfaces of a hot work tool steel. Int J Mater Res 2014;105:328–36. http://dx.doi.org/10.3139/146.111027.

[13] Rezayat M, Besharatloo H, Mateo A. Investigating the effect of nanosecond laser surface texturing on microstructure and mechanical properties of AISI 301ln. Metals 2023;13:2021. http://dx.doi.org/10.3390/met13122021.

[14] Hackel L, Rankin JR, Rubenchik A, King WE, Matthews M. Laser peening: A tool for additive manufacturing post-processing. Addit Manuf 2018;24:67–75. http://dx.doi.org/10.1016/j.addma.2018.09.013.

[15] Morgano M, Kalentics N, Carminati C, Capek J, Makowska M, Woracek R, Maimaitiyili T, Shinohara T, Loge R, Strobl M. Investigation of the effect of laser shock peening in additively manufactured samples through bragg edge neutron imaging. Addit Manuf 2020;34:101201. http://dx.doi.org/10.1016/j.addma.2020.101201.

[16] O'Brien J, Montgomery S, Yaghi A, Afazov S. Process chain simulation of laser powder bed fusion including heat treatment and surface hardening. CIRP J Manuf Sci Technol 2021;32:266–76. http://dx.doi.org/10.1016/j.cirpj.2021.01.006.

[17] Groenewold J, Hammes J, Stamer F, Lanza G. Influencing residual stress in PBF-LB/M Processes through in-process microstructure assessment and selective laser heat treatment. In: Beaman JJ, Kovar D, Cullinan M, Sha Z, Crawford R, Tilton M, editors. Proceedings of the 35th annual international SOLID FREEFORM fABRICATION SYMPOSIUM 2024. 2024, p. 1027–35. http://dx.doi.org/10.26153/tsw/58156.

[18] Hügel H, Graf T. Materialbearbeitung mit laser: Grundlagen und Verfahren. Wiesbaden: Springer Fachmedien Wiesbaden; 2022, http://dx.doi.org/10.1007/978-3-658-37252-1.

[19] Schüßler P, Damon J, Mühl F, Dietrich S, Schulze V. Laser surface hardening: A simulative study of tempering mechanisms on hardness and residual stress. Comput Mater Sci 2023;221:112079. http://dx.doi.org/10.1016/j.commatsci.2023.112079.

[20] Muthukumaran G, Babu P Dinesh. Laser transformation hardening of various steel grades using different laser types. J Braz Soc Mech Sci Eng 2021;43:103. http://dx.doi.org/10.1007/s40430-021-02854-4.

[21] Menold T, Onuseit V, Buser M, Haas M, Bär N, Michalowski A. Laser material processing optimization using bayesian optimization: a generic tool. Light: Adv Manuf 2024;5:1. http://dx.doi.org/10.37188/lam.2024.032.

[22] Chen C, Zeng X, Wang Q, Lian G, Huang X, Wang Y. Statistical modelling and optimization of microhardness transition through depth of laser surface hardened AISI 1045 carbon steel. Opt Laser Technol 2020;124:105976. http://dx.doi.org/10.1016/j.optlastec.2019.105976.

[23] Garnett R. Bayesian optimization. Cambridge, United Kingdom New York, NY, USA Port Melbourne, VIC, Australia New Delhi, India Singapore: Cambridge University Press; 2023, http://dx.doi.org/10.1017/9781108348973.

[24] Deng H, Gao P, Xiong H, Gao X. Experiments on resistance spot welding of three layers of unequal thickness steel based on deep learning and multi-objective optimization. CIRP J Manuf Sci Technol 2025;61:497–512. http://dx.doi.org/10.1016/j.cirpj.2025.07.005.

[25] Menold T, Onuseit V, Buser M, Haas M, Bär N, Michalowski A. Laser material processing optimization using bayesian optimization: a generic tool. Light: Adv Manuf 2024;5:1. http://dx.doi.org/10.37188/lam.2024.032.

[26] Kocijan J, Grancharova A. Application of Gaussian processes to the modelling and control in process engineering. In: Balas VE, Koprinkova-Hristova P, Jain LC, editors. In: Innovations in intelligent machines-5, vol. 561, Berlin, Heidelberg: Springer Berlin Heidelberg; 2014, p. 155–90. http://dx.doi.org/10.1007/978-3-662-43370-6_6.

[27] Cai W, Zhang Y, Zhou J. Maximizing expected model change for active learning in regression. In: 2013 IEEE 13th international conference on data mining. Dallas, TX, USA: IEEE; 2013, p. 51–60. http://dx.doi.org/10.1109/ICDM.2013.104.

[28] Silva VMA, Camerini CG, Pardal JM, Blás JCGD, Pereira GR. Eddy current characterization of cold-worked AISI 321 stainless steel. J Mater Res Technol 2018;7:395–401. http://dx.doi.org/10.1016/j.jmrt.2018.07.002.

[29] Asadi A, Abbasi M, Shamgholi M. Eddy current detection of retained austenite in Ni-Hard4 cast iron. Res Nondestruct Eval 2018;29:38–47. http://dx.doi.org/10.1080/09349847.2016.1221165.

[30] Shaira M, Guy P, Courbon J, Godin N. Monitoring of martensitic transformation in austenitic stainless steel 304 L by eddy currents. Res Nondestruct Eval 2010;21:112–26. http://dx.doi.org/10.1080/09349840903427854.

[31] Fricke LV. Using Eddy current technology for the determination of subsurface hardening during machining. [Ph.D. thesis], Garbsen: Gottfried Wilhelm Leibniz Universität Hannover; 2023.

[32] Todorov EI, Boulware P, Gaah K. Demonstration of array eddy current technology for real-time monitoring of laser powder bed fusion additive manufacturing process. In: Shull PJ, editor. Nondestructive characterization and monitoring of advanced materials, aerospace, civil infrastructure, and transportation XII. Denver, United States: SPIE; 2018, p. 40. http://dx.doi.org/10.1117/12.2297511.

[33] Spurek MA, Spierings AB, Lany M, Revaz B, Santi G, Wicht J, Wegener K. In-situ monitoring of powder bed fusion of metals using eddy current testing. Addit Manuf 2022;60:103259. http://dx.doi.org/10.1016/j.addma.2022.103259.

[34] Geľatko M, Hatala M, Botko F, Vandžura R, Hajnyš J. Eddy current testing of artificial defects in 316L stainless steel samples made by additive manufacturing technology. Materials 2022;15:6783. http://dx.doi.org/10.3390/ma15196783.

[35] Saddoud R, Sergeeva-Chollet N, Darmon M. Eddy current sensors optimization for defect detection in parts fabricated by laser powder bed fusion. Sensors 2023;23:4336. http://dx.doi.org/10.3390/s23094336.

[36] Spurek MA, Spierings AB, Lany M, Revaz B, Santi G, Wicht J, Wegener K. Influence of part temperature on in-situ monitoring of powder bed fusion of metals using eddy current testing. Prog Addit Manuf 2025;10:15–32. http://dx.doi.org/10.1007/s40964-024-00600-5.

[37] Bowler N. Eddy-current nondestructive evaluation. Springer series in measurement science and technology, New York, NY: Springer New York; 2019, http://dx.doi.org/10.1007/978-1-4939-9629-2.

[38] Schall R. The empirical coverage of confidence intervals: Point estimates and confidence intervals for confidence levels. Biom J 2012;54:537–51. http://dx.doi.org/10.1002/bimj.201100134.

[39] Hvarfner C, Hellsten EO, Nardi L. Vanilla Bayesian optimization performs great in high dimensions. In: Salakhutdinov R, Kolter Z, Heller K, Weller A, Oliver N, Scarlett J, Berkenkamp F, editors. Proceedings of the 41st international conference on machine learning. Proceedings of machine learning research, vol. 235, PMLR; 2024, p. 20793–817.

[40] Fanlin M, Xiucheng L, Heyun W, Cunfu H, Bin W. Characterization of elastic and plastic behaviors in steel plate based on eddy current technique using a portable impedance analyzer. J Sensors 2017;2017:1–12. http://dx.doi.org/10.1155/2017/8424012.

[41] Botko F, Zajac J, Czan A, Radchenko S, Simkulet V, Radic P, Bircak J. Preliminary study of residual stress measurement using eddy currents phasor angle. In: Hloch S, Klichová D, Krolczyk GM, Chattopadhyaya S, Ruppenthalová L, editors. Advances in manufacturing engineering and materials. Lecture notes in mechanical engineering, Cham: Springer International Publishing; 2019, p. 386–97. http://dx.doi.org/10.1007/978-3-319-99353-9_41.

[42] Botko F, Zajac J, Czan A, Radchenko S, Lehocka D, Duplak J. Influence of residual stress induced in steel material on eddy currents response parameters. In: Gapiński B, Szostak M, Ivanov V, editors. Advances in manufacturing II. Lecture notes in mechanical engineering, Cham: Springer International Publishing; 2019, p. 551–60. http://dx.doi.org/10.1007/978-3-030-16943-5_47.

[43] Bozorth RM. Ferromagnetism. Piscataway, N.J: IEEE Press; 1993.